Bubbles generated from wind-steepened breaking waves: 2. Bubble plumes, bubbles, and wave characteristics

Ira Leifer,[1] Guillemette Caulliez,[2] and Gerrit de Leeuw[3]

Received 19 August 2004; revised 19 August 2005; accepted 13 October 2005; published 16 June 2006.

[1] Measurements of breaking-wave-generated bubble plumes were made in fresh (but not clean) water in a large wind-wave tunnel. To preserve diversity, a classification scheme was developed on the basis of plume dimensions and "optical density," or the plume's ability to obscure the background. Optically dense plumes were due to the presence of a peak at large radius in the plume bubble size distribution. For each class, the plume formation rate, P, was measured at different fetches. The relationship between wave-breaking characteristics and the bubble plume evolution is examined in detail for these experiments. The wave-breaking rate and intensity were strongly fetch-dependent as the mechanically steepened wind waves rapidly evolved with fetch because of wind, dissipation, and nonlinear wave-wave interactions. P followed the trend in wave breaking, reaching a maximum at the fetch of maximum wave breaking. The ratio of dense to diffuse plumes was more sensitive to the wave-breaking intensity. Using P and the bubble population size distributions for each class, the global bubble plume injection size distribution, $\Psi_i(r)$, where r is radius, was calculated. Ψ_i decreased as $\Psi_i \sim r^{-1.2}$ for $r <$ 1700 μm and $\Psi_i \sim r^{-3.9}$ for larger r. Total volume injection was 640 cm^3 s^{-1}, divided approximately equally between bubbles smaller and larger than 1700-μm radius. Using plume volumes at maximum penetration for each class, a concentration distribution was calculated and showed plume concentrations greater than the background population by one to several orders of magnitude, depending upon r.

Citation: Leifer, I., G. Caulliez, and G. de Leeuw (2006), Bubbles generated from wind-steepened breaking waves: 2. Bubble plumes, bubbles, and wave characteristics, *J. Geophys. Res.*, *111*, C06021, doi:10.1029/2004JC002676.

1. Introduction

1.1. Bubble Plumes

[2] Bubbles from breaking waves either are dominant or significant to numerous diverse geophysical processes including air-sea gas transfer, turbulence generation, aerosol formation, sea surface microlayer enrichment, and the transformation of dissolved organic material to particulate organic material. Bubbles from breaking wind waves span a wide size range, from smaller than 20-μm [*Medwin and Breitz*, 1989] to 1.0-cm diameter [*Haines and Johnson*, 1995], covering a wide range of Reynolds numbers (0.05 to 4×10^3) and consequently a wide range of efficiencies for various bubble processes [*Clift et al.*, 1978]. Assessing the significance of a bubble-mediated process requires measurement of the bubble size distribution, which varies with many factors including wind speed [*Wu*, 1988], water temperature [*Asher and Farley*, 1995], and wave breaking mechanism (e.g., wave breaking due to wind stress, interaction with the bottom in the surf zone, or wave modulation). When measurements are time and spatially averaged, most of the bubbles observed are in the quasi steady state background population, which primarily consists of small bubbles. However, the source of the background population is the remnants of bubble plumes that have a distinctly different size distribution. Plume populations contain many large bubbles, have much higher bubble concentrations, and are transient. While for some processes the background population is the most important (e.g., acoustic scattering), plume bubbles may dominate for others (e.g., soluble gas transfer). To date, few observations exist for bubble plumes. Of these, even fewer are time resolved of what is a dynamic and rapidly changing phenomena.

[3] In this paper and its companion paper *Leifer and De Leeuw* [2006] (hereinafter referred to as LD) we present observations of bubble plume characteristics and generation rates made with a bubble measurement system for bubble plumes formed by wind-amplified, mechanically generated breaking waves in a large wind-wave channel. After an extensive review of the various processes in which bubble plumes are involved at the air-sea interface and of previous related studies, a summary is presented of observations of ~3500 bubble plumes. LD present a detailed study of a subset of these plumes.

[1] Marine Science Institute, University of California, Santa Barbara, California, USA.
[2] Institut de Recherche sur les Phenomenes Hors Equilibre, Marseille, France.
[3] TNO Physics and Electronics Laboratory, The Hague, Netherlands.

0148-0227/06/2004JC002676

[4] Herein we explore the variability in the formation rate for different bubble plume classes with respect to wave development on the basis of these wind tunnel observations. Wind tunnels allow detailed measurements to be made from stable platforms, but are on a much smaller scale than oceanic conditions. Thus their finite dimensions prevent tunnels from even *approaching* swell typical to the ocean or the turbulent kinetic energy input from the oceanic-scale dominant breaking wavelengths. However, the wavelengths responsible for wave breaking and plume formation are generally significantly shorter than the dominant wind waves, that is, waves of the spectral peak and swell [*Gemmrich and Farmer*, 1999; *Dulov et al.*, 2001]. Moreover, wave breaking and bubble plume formation occur on very short timescales, less than 0.1 s (LD). Although bubble velocities during injection can be up to $\sim$1 m s^{-1}, we argue that for the formation process, the tunnel dimensions are sufficiently large to prevent boundary effects from being dominant, and moreover, that the processes of bubble plume formation from wave breaking in the ocean and lab exhibit similarities (but likely also differences).

1.2. Bubble-Mediated Processes

[5] Bubbles from wave breaking both directly and indirectly enhance the atmosphere-ocean exchange of gases such as carbon dioxide, methane, and fluorocarbons, which are all important to global climate. As a result, field measurements of gas exchange versus wind speed show an increase in efficiency above the wind speed where wave breaking and bubble formation begin [*Wanninkhof*, 1992], which introduces a solubility dependency [*Woolf*, 1993]. Entrained air outflows from the bubbles (invasion) while dissolved gas from the ocean inflows into the bubble (evasion). The bubbles then release their contents to the atmosphere upon bursting at the surface [*Woolf*, 1997]. Bubbles also indirectly contribute to gas exchange by disrupting the surface microlayer [*Liss et al.*, 1997] and generating turbulence in the upper ocean [*Thorpe*, 1982]. It follows that bubbles are potentially important for the process of surface renewal and thus gas exchange. In fact, turbulence generation and bubble plume formation from wave breaking are linked inextricably. After formation, the two interact during all phases of their evolution. By altering the turbulence-velocity profile within the oceanic boundary layer, bubbles indirectly enhance gas transfer [*Kitaigorodskii*, 1984]. Bubble plumes also induce bulk-fluid motions, such as the upwelling flow [*Asher et al.*, 1997; *Leifer et al.*, 2000b], which can enhance gas transfer by altering the concentration profile near the interface.

[6] Air-sea gas exchange and momentum transfer occur across the surface microlayer and are strongly influenced by the presence of surface slicks [*Liss et al.*, 1997], which damp capillary waves. Both wave breaking and the surfacing and bursting of bubbles at the air-sea interface disrupt the surface microlayer [*Liss et al.*, 1997] bringing fresh water to the interface. Because typically the surface microlayer is cooler than the bulk water, processes that disrupt the microlayer (bubbles and wave microbreaking or breaking) change the skin temperature [*Gemmrich*, 2000]. Bubbles also affect upper ocean optics and thus the sea color [*Flatau et al.*, 2000].

[7] As they rise, bubbles efficiently collect surface-active substances, surfactants, that are advected by the flow around the bubble to the downstream bubble hemisphere [*Sadhal and Johnson*, 1983; *Fdhila and Duineveld*, 1996]. The bubble then transports the surfactants to the air-water interface where they are released upon bursting. This process, known as sparging, is the core process of wastewater treatment microflotation [*Persechini et al.*, 2000; *Deglon et al.*, 1999], mining airlift separators [*Mao and Yoon*, 1997], and bioreactors [*Van der Pol et al.*, 1995; *Wu*, 1995]. In the ocean, bubble accumulation of surfactants contributes to aggregate formation and flocculation [*Baylor and Sutcliffe*, 1963; *Johnson et al.*, 1986; *Mopper et al.*, 1995; *Mari*, 1999; *Cincinelli et al.*, 2001] and may be important to the formation of colloidal material [*Kepkay*, 1991] and transparent exopolymer particles (TEP). TEP are formed from exuded polysaccharides [*Alldredge et al.*, 1993; *Passow*, 2000]. Found in high abundance in many algal blooms [*Passow et al.*, 1994], TEP enhance aggregate formation [*Alldredge et al.*, 1993; *Dam and Drapeau*, 1995] and increase sedimentation rates, particularly during the terminal phase of algal blooms [*Alldredge and Gotschalk*, 1990]. Thus bubbles provide an efficient "nucleation" site for organic particle aggregation and formation, potentially playing a significant role in global cycling of dissolved organic carbon to particulate organic carbon [*Monahan and Dam*, 2001].

[8] When present, bubbles are an important and potentially dominant mechanism for maintaining an enhanced sea surface, surfactant microlayer concentration [*Grammatika and Zimmerman*, 2001; *Cincinelli et al.*, 2001]. The sea surface microlayer is particularly important to transfer processes between the atmosphere and the bulk fluid. Surfactant concentrations in the microlayer, both particulate and molecular, generally are enhanced relative to the bulk fluid [*Mopper et al.*, 1995; *Cini and Loglio*, 1997]. Surfactant films decrease wave development as well as heat, momentum, and mass transfer [*Liss et al.*, 1997]. At the same time, both wave breaking and bubble bursting disrupt the surface microlayer, removing surfactants from the microlayer [*Cincinelli et al.*, 2001]. Part of these surfactants are ejected into the atmosphere as aerosols [*Blanchard*, 1989]. A recent study of aerosol chemical composition at the coast of Mace Head, Ireland, showed that a very large fraction of the aerosol components consists of organic material [*O'Dowd et al.*, 2004].

[9] Bursting bubbles are a major source for sea spray aerosols at low to intermediate wind speeds [*Monahan*, 1986; *De Leeuw*, 1990; *Spiel*, 1998]. Sea-salt aerosol production spans a wide size range, from 20 nm [*Mårtensson et al.*, 2003] to larger than 100 μm [*De Leeuw*, 1993], and these aerosols are the dominant submicrometer scatterers in most ocean regions. They dominate the particulate mass concentration of the marine boundary layer in remote oceanic regions, with a significant fraction occurring in the submicrometer size range [*Intergovernmental Panel on Climate Change*, 2001]. At lower altitudes in the atmosphere, sea spray aerosols can dominate atmospheric propagation at visible and infrared wavelengths. Also, sea spray aerosols are the primary contributors to the indirect aerosol effect (IAE), the most uncertain forcing mechanism in the prediction of climate change. The IAE arises from aerosols' importance to the formation of marine stratocumulus clouds. *Boers et al.* [1998] reported an example of IAE

related to changes in the distributions of natural cloud condensation nuclei over the ocean, while *O'Dowd et al.* [1999a, 1999b] demonstrated that sea spray aerosols can play a significant role in marine stratocumulus microphysics and chemistry. In addition, sea spray aerosols can provide a significant sink for natural and anthropogenic trace gases [*O'Dowd et al.*, 2000].

[10] Sea spray aerosols can be enriched significantly in oceanic viruses [*Blanchard*, 1989; *Van Dolah et al.*, 2001], bacteria and fungi [*Marks et al.*, 2001], red tide toxins [*Grzebyk et al.*, 1997; *Pierce et al.*, 1990, 2005; *Rumbold and Snedaker*, 1999], and pollutants [*Cincinelli et al.*, 2001], and thus play an important role in transport of these substances in coastal zones. Epidemiological studies have shown increased incidence of respiratory diseases correlated with whitecapping and aerosol transport [*Backer et al.*, 2003]. Also, sea spray aerosols enhance deposition of some compounds. The sea-salt displacement reaction, where sea spray aerosols uptake nitric acid while releasing hydrochloric acid, shifts nitrogen from fine to coarse aerosols, thereby enhancing the deposition flux of nitrogen while simultaneously the flux decreases with respect to the gas phase flux [*De Leeuw et al.*, 2003].

1.3. Importance of Different Size Regimes

[11] Buoyant rise rapidly returns most plume bubbles to the surface; however, some bubbles diffuse out of the plume (or remain behind) forming a (comparatively) quasi steady state background population. These two populations, the background and plume populations are quite different. Within the plume, the bubble size distribution is weakly size dependent and thus plumes contain a significant number of large bubbles [*Haines and Johnson*, 1995]. We define the transition between small and large bubbles at an equivalent spherical radius, r, of 700 μm, which is the onset of oscillations at 20°C in quiescent water [*Leifer et al.*, 2000a]. Small bubbles are spherical ($r < 300$ μm) or ellipsoidal ($300 < r < 700$ μm) and rise linearly, while large bubbles are irregular in shape and exhibit both trajectory and shape oscillations [*Leifer et al.*, 2000a]. In seawater, small bubbles generally behave hydrodynamically dirty because of surfactant contamination, while large bubbles generally behave hydrodynamically clean [*Patro et al.*, 2002]. Bubble surfactant contamination is important to many bubble-mediated processes such as gas exchange [*Clift et al.*, 1978] and aerosol production [*Spiel*, 1998].

[12] Bubble lifetimes for these two populations are very different. Consequently, these two populations affect various bubble-mediated geophysical processes differently. The predominantly small, background bubbles rise slowly and thus have long subsurface lifetimes, particularly in the highly turbulent environment produced by breaking waves [*Woolf*, 1993]. In contrast, the large bubbles in the bubble plume rise rapidly and thus have lifetimes on the order of seconds [e.g., *Haines and Johnson*, 1995]. Also, the rising mass of plume bubbles creates an upwelling flow [*Asher et al.*, 1997] that transports many smaller and larger bubbles more rapidly to the surface [*Leifer*, 1995]. The background population decreases exponentially with depth [*Wu*, 1988]. By contrast, the intense turbulence of the bubble plumes causes time-resolved plume populations to be comparatively homogeneous, that is, well mixed [*Haines and Johnson*, 1995].

[13] Many bubble processes show a strong size dependency with very different behavior for small and large bubbles. For example, the rise velocity, V_B, for small bubbles varies significantly with r, while V_B varies only weakly with r for large bubbles [*Leifer et al.*, 2000a]. Other processes with strong size dependencies include gas exchange [*Leifer and Patro*, 2002] and aerosol production efficiencies [*Spiel*, 1998]. Thus assessing the relevance of bubbles to a geophysical process requires consideration of the appropriate size range and bubble population, particularly since bubble measurement systems operate over limited size ranges [*Leifer et al.*, 2003].

2. Previous Time- and Space-Averaged Bubble Measurements

[14] Most bubble measurements are time and space averaged, and thus heavily biased toward bubbles outside of bubble plumes. Bubble size distributions in the ocean and laboratory are measured primarily by acoustic, optical (photo or video), or laser methods, with each having advantages and disadvantages [*Vagle and Farmer*, 1998; *Leifer et al.*, 2003]. Video systems can measure bubbles with both regular and irregular shapes even at high void fraction. Both acoustic and laser methods require low void fractions and regularly shaped bubbles (spherical or ellipsoidal) for correct sizing, that is, $r < 700$ μm in stagnant water; smaller in turbulent environments. Acoustical methods are best for low void fractions, 10^{-5} being a typical upper limit for backscatter sonar [*Vagle and Farmer*, 1998]. Laser systems require no more than one bubble in the measurement volume at a time, and consequently are limited to low bubble densities. Acoustic methods can measure noninvasively over large spatial domains but not near the sea surface. Multiple frequency approaches can measure size distributions [*Medwin and Breitz*, 1989]; however, simpler single frequency approaches can yield the spatial (horizontal and vertical) distribution of the total bubble number [*Crawford and Farmer*, 1987]. Video can operate at very high bubble densities; however, automated image-processing routines function best where bubble images do not overlap. Although automatic analysis is feasible for some overlap [*Leifer et al.*, 2003], significant bubble overlapping requires manual bubble identification [*Haines and Johnson*, 1995; LD].

[15] A summary of published oceanic and laboratory background bubble measurements is provided in Table 1. Size ranges are not reported for single frequency acoustic measurements. The size dependency of the bubble distributions shows enormous variability, although most measurements show a power law dependency, with the exponent, S defined by

$$\phi(r) = kr^{-S} \tag{1}$$

where ϕ is the bubble concentration size distribution and k is a constant. Values of S are calculated from a least squares, linear regression analysis of the logarithm of equation (1), that is,

$$\log(\phi) = -S\log(r) + \log(k) \tag{2}$$

over an appropriate range of r.

Table 1. Summary of Background Bubble Observations[a]

Reference	S	r, μm	Type	Location	Depth, cm	U_{10}
Blanchard and Woodcock [1957]	4.7	375–750	Bubble trap	Ocean	10	
Kolovayev [1976]	4	50–400	Optical	Ocean	150–800	11–13
Johnson and Cooke [1979]	4.5	50–170	Bubble trap	Ocean	70–400	8–13
Walsh and Mulhearn [1987]	2.9:6.0	51–300	Photo (f-stop-22)	Ocean	60–170	8–14
Baldy and Bourgüel [1987]	2:4	50–3000	Laser PDA	LUMINY(f)	45:8.5	14
Crawford and Farmer [1987]	–	–	Acoustic	Ocean	–	9–11
Baldy [1988]	2:4	50–1500	Laser PDA	LUMINY(f)	10:–8.5	14
Medwin and Breitz [1989]	~4	30–240	Acoustic (multi)	Ocean	25	12–15
Hwang et al. [1990]	2:4.5	350–1100	Laser blocking	Wind wave(f)	3–12	10–16
Vagle and Farmer [1992]	N/A	70–150	Acoustic	Ocean	50–730	11
Cartmill and Su [1993]	3	200–1200	Acoustic (multi)	Wind wave	30	–
Asher and Farley [1995]	N/A	30–500	Laser PDA	WST(s)	25–50	–
Terrill et al. [2001]	3:5	30–800	Acoustic	Ocean	70–410	15
De Leeuw and Cohen [2002]	1.8:5.7	15–500	Video	Ocean	30	5–13
Graham et al. [2004]	N/A	10–100	Acoustic (3 freq)	Ocean	–	5–12

[a]S is the power law dependency of the distribution, defined in (1); r is the bubble radius; and U_{10} is 10-m wind speed or reported u for the wind tunnel. N/A indicates not provided in manuscript, and PDA is laser phase Doppler anemometer.

[16] Bubble size distributions observed in the ocean, in wind wave tunnels and from tipping bucket experiments show significant variability, particularly in more recent measurements. There are numerous sources of variability, including temperature [*Asher and Farley*, 1995; *De Leeuw and Cohen*, 2002], salinity [*Cartmill and Su*, 1993; *Haines and Johnson*, 1995; *Asher et al.*, 1997], wave development [*Walsh and Mulhearn*, 1987; *De Leeuw and Cohen*, 2002], dissolved gas concentrations [*Stramska et al.*, 1990], atmospheric stability [*De Leeuw and Cohen*, 2002], wind speed [*Crawford and Farmer*, 1987; *De Leeuw and Cohen*, 2002], and surfactants [*Asher et al.*, 1997]. These differences result not only from variability in formation mechanism (e.g., LD) but also the time evolution of the bubble plume since the bubble behavior (rise speed and gas exchange) depends upon many of these factors [*Thorpe et al.*, 1992]. Additionally, the location of the measurement is important since size distributions decrease sharply with depth [*Wu*, 1988] and distance from bubble plumes [*Baldy and Bourgüel*, 1987].

[17] Finally, different measurement techniques create additional challenges to comparisons [*Vagle and Farmer*, 1998; *Leifer et al.*, 2003]. Typically, optical measurements show a spectral peak at 60 μm or near the small size limit of the optical instruments if the resolution size limit is larger than 60 μm. The distribution then decreases sharply with decreasing r [e.g., *Johnson and Cooke*, 1979]. This is in direct contradiction to acoustical observations which show a continuation of the power law description of the distribution to as small as 10 μm radius [e.g., *Medwin and Breitz*, 1989] or peaked at 20 to 30 μm [*Vagle and Farmer*, 1992]. Optical bubble measurements by *De Leeuw and Cohen* [2002] with a lower cutoff at $r \sim 10$ μm showed a clearly resolved peak at 60 to 100 μm, with a minimum at 30 μm and a second peak near the small size limit. On the basis of laboratory studies, *Leifer et al.* [2000c] proposed the small peak was due to bubbles produced during the bubble-bursting process.

[18] Measurements close to the region and time of bubble formation have smaller S (i.e., the size distribution is less strongly size dependent) than those further away [*Baldy*, 1988; *Medwin and Breitz*, 1989; *Leifer*, 1995]. *Baldy and Bourgüel* [1987] and *Baldy* [1988] used a laser to look at bubbles very close to the interface including between the wave crest and trough, and found S decreased from 4 at the level of the trough to either 2 or 2.5 in the wave crest. *Hwang et al.* [1990] observed a similar decrease with decreasing depth in S from 4 to 2 using a laser light blocking technique. *Terrill et al.* [2001] used an acoustic system and saw a decrease in S from 5 to 3 with proximity to the sea surface. *Kolovayev* [1976] found S was 4 at several meters depth for high wind speeds. *Vagle and Farmer* [1992] also observed S to decrease with decreasing depth, from 8 to 1.

[19] *Walsh and Mulhearn* [1987] used a camera in the ocean over a wide range of wind speeds and found S varied widely depending upon factors including wave development (short fetch yielded less bubbles). Their average value for S was 4, in precise agreement with S for acoustic measurements by *Medwin and Breitz* [1989]. However, *Walsh and Mulhearn* [1987] did not find a clear trend with the 10-m wind speed, U_{10}. *Crawford and Farmer* [1987] used acoustic observations referenced to the size distributions of *Johnson and Cooke* [1979] to characterize bubble plumes and total bubble concentration. They found that total concentration had a wind speed dependency of $U_{10}^{3\pm0.3}$, while *Wu* [1988] proposed a wind speed dependency of $U_{10}^{3.5}$ on the basis of data from *Kolovayev* [1976], *Johnson and Cooke* [1979], and *Thorpe* [1982]. *Crawford and Farmer* [1987] found that plume width decreased rapidly with depth; thus at least part of the reason that spatially averaged measurements show lower bubble concentrations at greater depths is because plumes are narrower and shorter lived at greater depths. *Graham et al.* [2004] used a three-frequency acoustic system to look at bubbles in a shallow sea (20 m) and observed that bubble penetration varied inversely with wave age (c/U_{10}) where c is the wave phase speed; that is, older waves created deeper plumes.

[20] Perhaps the most extensive set of published oceanic size distributions was by *De Leeuw and Cohen* [2002] covering seven different cruises in the North Atlantic and the North Sea. This data set has the advantage of using the same (optical) instrument and data processing method. Measurements were made for a wide range of conditions (temperature, atmospheric stability, wind speed, and surfactant load) and showed S ranged from 1.8 to 5. The differences between the results from the various deployments were attributed to the measurement depth, wind speed, fetch

(i.e., wave development), as well as seasonal variations. Bubble measurements in the Pacific showed a change in the size distribution with U_{10}. Bubble concentrations increased by two orders of magnitude for an increase in U_{10} from 6 to 12 m s^{-1} with the main spectral peak shifting to larger r. In general, peak concentrations were greater with higher U_{10}, but distributions were steeper. Furthermore, the bubble distributions for water temperatures spanning 8°C to 28°C showed that the small bubble concentration decreased with increasing water temperature, while concentrations for bubbles larger than $r \sim 70$ μm increased with increasing water temperature. These results demonstrate the importance of environmental parameters on bubble formation and the size distribution evolution. They also demonstrate that only some of the variability between different researchers can be explained by different experimental methodologies.

[21] Salinity is a significant factor in bubble formation. In whitecap simulation tank (WST) experiments, *Haines and Johnson* [1995] showed a similar power law exponent for large bubbles in fresh and salt water (S = 2.7, S = 2.6, respectively); however, the spectral peak was at much larger r for fresh ($r \sim 2800$ μm) than salt ($r \sim 630$ μm) water. Small ($300 < r < 600$ μm) bubble concentrations were much larger in salt water than fresh water, while large ($r >$ 2000 μm) bubble concentrations were greater in fresh water. From laser bubble measurements in a WST, *Asher et al.* [1997] observed a similar slope in ϕ for salt and fresh water (S unreported); with higher concentrations for small, salt-water bubbles. The freshwater ϕ had a peak or a plateau at 500 μm, and as a result the freshwater concentration of bubbles larger than $r \sim 200$ μm was greater than for salt water. Part of the discrepancy between these two data sets may have resulted from wall effects. For bubble measurements in a WST, *Haines and Johnson* [1995] indicated wall effects may have been significant, although the WST used by *Asher et al.* [1997] was much larger. For mechanically generated, breaking-wave bubble plumes, *Loewen et al.* [1996] found that for larger bubbles ($1000 < r < 4000$ μm), there was little difference between fresh and salt water for focused waves. For wind-generated breaking waves, *Cartmill and Su* [1993] showed that for $50 < r < 1000$ μm, far more small bubbles (an order of magnitude) were produced in saltwater than freshwater. To summarize, the wave breaking observations are in general agreement with the WST results, that is, that the fresh and salt water distributions of larger bubbles are similar, but with far more small bubbles produced in salt water. Since most of the plume mass is in the large bubbles, total gas injection appears to be largely independent of salinity [*Wu*, 2000].

[22] Wave breaking and associated fluid motions likely are the major factors that influence both bubble formation and subsequent transport in the water (surface currents could also play a role). In turn, wave breaking is affected by fetch [*De Leeuw and Cohen*, 2002], air-sea temperature difference (i.e., boundary layer stability) [*Spillane et al.*, 1986], and slicks [*Asher et al.*, 1997], among other factors. For example, factors that affect surface stress, such as the angle between the wind and wave direction or surface currents also likely affect wave breaking and thus bubble formation; however, the dependency of bubble production on these and other variables remains largely unquantified. Efforts to relate whitecap coverage to wind speed or friction velocity show enormous variability [e.g., *Monahan*, 1986], some of which is certainly due to these factors.

Table 2. Bubble Plume Classification Criteria[a]

Type	Symbol	Criteria
Broad	B	$w > 30$ cm
Narrow	N	$w < 30$ cm
Shallow	S	$z_p < 15$ cm
Deep	D	$z_p > 15$ cm
Dense	De	For $t < 1$ s, bubbles obscure background
Diffuse	Di	For $t < 1$ s, background not obscured
Micro	Narrow shallow diffuse	$w < 10$ cm, $z_p < 10$ cm, $N < 100$ (μm^{-1})

[a]Here w is width, z_p is penetration depth, t is time, and N is number of bubbles.

3. Methods

[23] The LUMINY experiment described by *De Leeuw et al.* [2002], hereafter referred to as LUMINY, is described by LD. In brief, bubble plume populations, plume characteristics, gas transfer rates, and wind and wave conditions were measured in the large wind-wave channel at the Institut de Recherche sur les Phenomenes Hors Equilibre in Marseilles, France. The wind-wave channel is 2.5 m high by 2.6 m wide by 40 m long and was filled with 0.9 m of fresh water. Although the tap water was filtered and exposed to UV radiation during the tank filling, the water quality decreased rapidly and was not clean during these experiments. Water temperatures were between 14°C to 18°C. Bubbles were measured during experiments with a wind speed of 13 m s^{-1} and wave-maker paddle waves with a wavelength of 1.3 m and a frequency of 1.2 Hz. Average wave height was ~12 cm at the measurement fetches. The National University of Ireland, Galway (NUIG) bubble measurement system (BMS) is described by *Leifer et al.* [2003]. This BMS used three video cameras to measure bubbles simultaneously in multiple locations and over a size range from $r \sim 150$ μm to $r \sim 7000$ μm, the largest bubble observed. The BMS overview camera had a wide field of view that provided contextual information of plume structure and dynamics.

[24] Using overview camera images, a plume classification scheme, which is described by LD (see Table 2), was used to segregate bubble plumes. The scheme was based on the bubble plume horizontal extent, w, penetration depth z_p, and optical image density. Deep plumes had $z_p > 15$ cm, while narrow plumes had $w < 30$ cm. Dense plumes were able to obscure most of the background until at least maximum penetration. Dense plumes had a significant population of large bubbles (LD). Very small shallow, narrow and diffuse plumes were classified as microplumes (see Table 2). On the basis of the plume classification scheme, bubble plumes for each plume class were analyzed and the overall plume-class characteristics (penetration depth, lifetime) and bubble population characteristics (modes, size distribution, and total bubble volume) were determined. Overview images of each plume class are shown in Figure 1.

[25] The plume generation rate, P, for each plume class was determined from digitized video clips, ~2 min long, for a range of fetches during two experiments with the same wind and wave conditions (13 m s^{-1} wind and paddle waves). P was normalized to per unit surface area and per

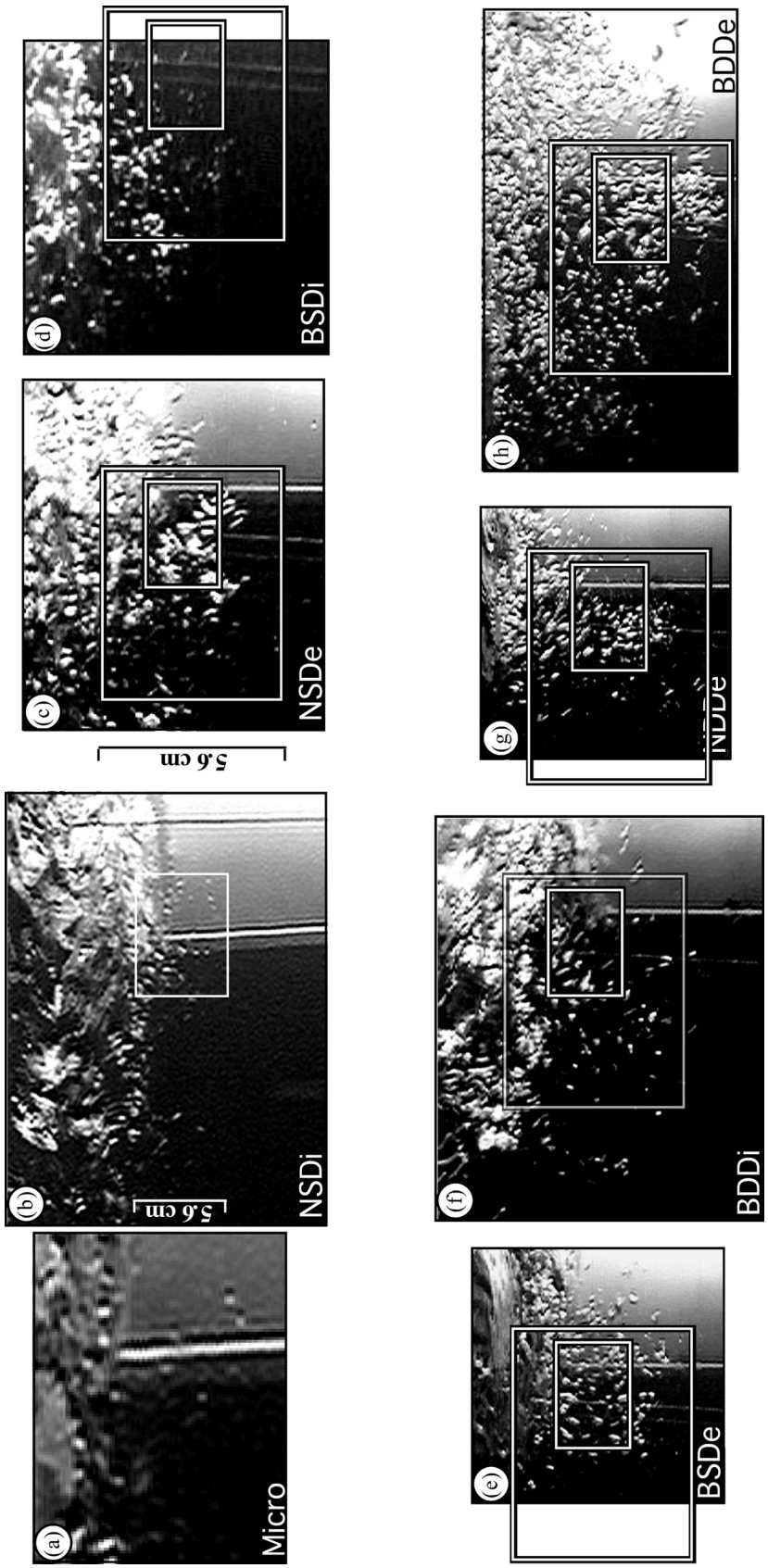

Figure 1. Overview images of each bubble plume class, including narrow and wide FOV cameras: (a) microplume, (b) NSDi, (c) NSDe, (d) BSDi, (e) BSDe, (f) BDDi, (g) NDDe, and (h) BDDe. See text for more on each plume class. Size scale for Figure 1b is shown in the figure. Size scale for Figures 1a and 1c–1h is shown in Figure 1c.

second on the basis of the video clip length and analysis region. Only plumes in a subset area of the overview camera's field of view (FOV) were analyzed. The region extended from the interface visible nearest the camera (~20 cm distant) to the illumination screen (90 cm distant), and from the illumination screen edge (pixels of the screen were saturated, thus plumes were not visible) to the FOV edge in the upstream direction (~1 m). More distant plumes were visible and were identified as outside the measurement region since they were not back illuminated. Plume dimensions were estimated relative to the illumination screen for bubble plumes at the furthest edge of the measurement region, or the wave gauge wires if located within the closer half of the measurement region. Thus plume dimensions were approximate, with an estimated size uncertainty of ~15%. However, this uncertainty only affects the classification of plumes whose size was close to the threshold between classes, that is, a small fraction of the plumes.

[26] Of greater concern was the subjective aspect of this analysis, specifically, that during the course of the analysis, the criteria discriminating between the classes could shift. To address this issue, one clip was analyzed twice, once at the beginning of the analysis, and then several days later, after the analysis was finished. Consistency was lowest for microplumes with agreement for P between the two analyses of 85%. Agreement for other plume classes was 90% or better. The two consistency analyses were averaged together.

[27] The wave field was analyzed from time series of the wave height measured by a high-resolution, capacitance wave gauge located at the downstream edge of the camera's field of view. The wave data were synchronized with the video camera records. Fully breaking waves were detected from these wave signals by using a geometric criterion as described by *Longuet-Higgins and Smith* [1983] and *Caulliez* [2002]. In brief, an individual wave was considered as breaking when the water surface slope at the crest exceeded 0.586 in magnitude or 30° in angle. In this work, only fully developed breaking waves characterized by steep but corrugated ''turbulent'' wave fronts in which the wave slope presents several peaks crossing the threshold value and separated from each other by very short time intervals, were considered. Instantaneous water slopes were evaluated from the ratio between the time derivative of the wave height signal and the mechanical water-wave phase speed determined by a cross-correlation method.

4. Bubble Plume Characteristics

4.1. Bubble Plume Life Cycle

[28] The life cycle of bubble plumes generated by breaking wind waves encompasses four phases: formation, injection, rise, and senescence. Formation of bubble plumes includes bubble fragmentation and lasts less than 0.1 s. Injection follows formation during which the plume bubbles descend (i.e., are injected) below the surface. Injection ends when the plume reaches their maximum penetration, z_p, and the rise phase begins. During the rise phase, bubbles buoyantly rise toward the surface. Smaller bubbles, typically $r <$ 200 μm, that remain in the water after the main body of plume bubbles has surfaced, comprise the senescence phase. During senescence, turbulence diffusion and wave orbital motions are important.

Table 3. Bubble Plume Class Characteristics[a]

Class	t, s	z_p, cm	$\langle B_V \rangle$, cm^3	B_{VM}, cm^3	P_{VM}, cm^3
Micro[b]	0.4	3.2	0.15	0.4	18
NSDi[b]	0.7	6	0.44	0.8	120
BSDi	0.6	6	0.88	1.8	300
BDDi	1.2	18	0.47	1.1	1200
NDDi	1.2	18	0.47	1.1	1200
NSDe[b]	0.9	9	1.9	3.8	460
BSDe	1.0	12	3.5	4.9	2400
NDDe[b]	1.2	23	2.8	4.8	2400
BDDe[b]	1.5	33	5.2	33.	10,000

[a]Here τ is the plume lifetime, z_p is the maximum penetration depth, $\langle B_V \rangle$ is the total mean bubble volume over τ, and B_{VM} and P_{VM} are bubble and plume volumes at the maximum of plume penetration. For further details, see LD.
[b]These are noninteraction classes.

4.2. Plume Classes

[29] Bubble population size distributions, Φ, were determined for plumes in each plume class and are summarized in Table 3 for late injection/early rise phase, further details are presented by LD. Φ is the total number of bubbles in the plume in each size class and is roughly conserved during injection, while concentration decreases as the plume expands. Differences between plume concentration and population size distributions are discussed by LD.

[30] Microplumes were the most common plume class observed. Microplumes generally were observed forming in the trough rather than the crest. The microplume injection Φ was weakly size dependent until $r \sim 1000$ μm, with a steep decrease for larger bubbles.

[31] Of the diffuse plumes larger than micro, NSDi plumes were the most common. NSDi plumes were similar in several respects to microplumes. For example, plume lifetime, τ, was approximately the same for both ($\tau \sim 0.6$ s). Also, for both, the injection Φ were weakly r dependent for $r < \sim$1000 μm, decreasing steeply for larger r. Because of their greater z_p, large bubbles in NSDi plumes remained submerged longer; thus the average plume bubble volume, $\langle B_V \rangle$, and maximum plume bubble volume, B_{VM}, differed to a lesser extent than $\langle B_V \rangle$ and B_{VM} for microplumes. Since Φ decreased shallowly for $r < 1000$ μm and steeply for $r > 1000$ μm with a power law exponent, $S > 3$, bubbles with $r \sim 1000$ μm contained most of the bubble volume. All other diffuse plumes were interaction plumes, discussed below.

[32] Very different types of plumes were observed which were termed dense because of their ability to obscure optically the background. The smallest and most common dense plume class was NSDe, which, like other dense plumes, had greater large bubble Φ relative to small bubble Φ than diffuse plumes. For NSDe plumes, τ was longer than for NSDi plumes despite comparable dimensions. Much larger plumes were observed and had significantly greater Φ, but were much less common than shallow plumes. Despite their less frequent occurrence, because of their greater Φ, deep dense plumes were neither dominant nor negligible contributors to the global bubble formation rate. The deep, dense plumes persisted the longest, with τ varying from 1 to 1.5 s and had greater z_p. Consequently,

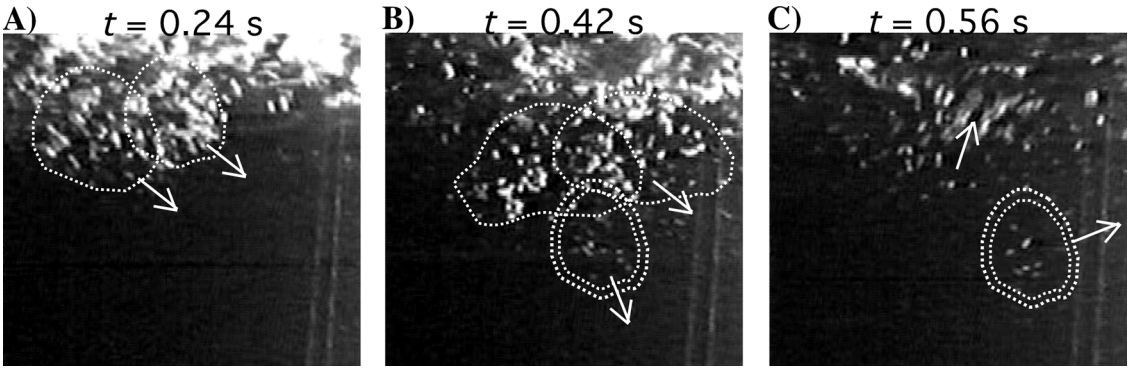

Figure 2. Image sequence showing formation of a BDDi plume due to the interaction of two NSDi plumes. Single dotted white line demarcates individual plumes; double dotted white line denotes a portion of the plume injected deeper. Time t is after formation.

these plumes produced many more senescence bubbles at greater depths (deeper than the wave height) and thus contributed significantly to the deeper background bubble population. The largest plumes of all were BDDe which occurred very infrequently and were significantly larger than NDDe plumes.

[33] Several plume categories resulted from the interaction of two plumes in close proximity. The deep interaction classes (BDDi and NDDi) occurred very infrequently. An example of the formation of a BDDi plume is shown in Figure 2. The two NSDi plumes are circled by dashed lines. Because of the interaction between the plumes, a group of bubbles, outlined by a double dotted line in Figure 2b, continued descending while most of the bubbles in the NSDi plumes were already rising. The two NSDi plumes formed closely in time (time lag of ~40 ms) and were separated by only a few centimeters. Not all plume interactions produced large plumes and the conditions for constructive interaction remain unclear. Most NSDi plumes were produced singly from a single wave, but occasionally a wave produced a series of NSDi plumes. In this case, some of these NSDi plumes interacted. The three diffuse interaction plume classes (BSDi, NDDi, and BDDi) had Φ similar to NSDi plumes. The deep interaction classes, BDDi and NDDi plumes also had longer τ (~1 s). In a similar manner, the shallow interaction classes, BSDe, resulted from two NSDe plumes forming in sufficiently close proximity and time and thus Φ for BSDe plumes were similar to Φ for NSDe plumes. Example overview video for the NSDi and BDDE plume shown in Figure 1 are available in the auxiliary material[1].

5. Wave Development

[34] Even if little is known on the detailed mechanisms involved and the exact relationship between the phenomena, bubble plume generation is undoubtedly dependent on wave development and the associated wave-breaking occurrence and intensity. For observations made in the tank with wind and mechanical waves, the wave field did not reach energy equilibrium with wind at the fetches where observations were taken (17.5–30 m). This was indicated by the fact that wind input to mechanical waves did not equilibrate exactly with nonlinear transfer or energy loss by breaking. It follows that a fetch dependency was expected in the bubble generation rates and more interestingly, in the formation probability of the different bubble plume classes. Therefore a careful investigation of the wave development with fetch was conducted in conjunction with the bubble measurements.

[35] The wave development along the tank was first described by the evolution with fetch of the averaged trough-to-crest height, H, for the same experiments as the bubble plume studies, for example, 13 m s^{-1} wind speed and paddle waves (Figure 3). This quantity exhibited a well-marked variation with fetch, initially growing slowly, reaching a maximum between 22- and 24-m fetch and then decreasing significantly before increasing again at 30 m. This evolution also was well representative of the trend in wave steepness because for mechanical waves, the variation in frequency and wavelength along the tank was negligible. For these wind and paddle wave conditions, wave breaking started at 10- to 12-m fetch. However, particularly intense wave breaking occurred at clearly distinguishable fetches, generally between 21 and 24 m. In this region, the percentage of breaking waves reached a well-peaked maximum of ~35% (Figure 4a). Immediately downstream, the breaking rate decreased markedly, indicating that the intense wave field energy loss by wave breaking was not entirely compensated by direct input of wind energy. By 30 m, the

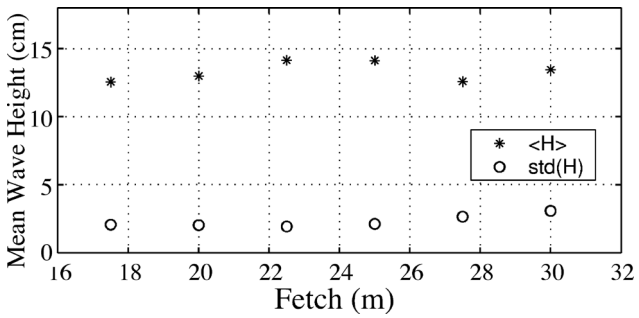

Figure 3. Fetch variation of the average trough-to-crest wave height H (asterisks) and the standard deviation (circles) as estimated from the wave signal recorded contemporaneously with the bubble plume observations.

[1]Auxiliary material is available at ftp://ftp.agu.org/apend/jc/2004jc002676.

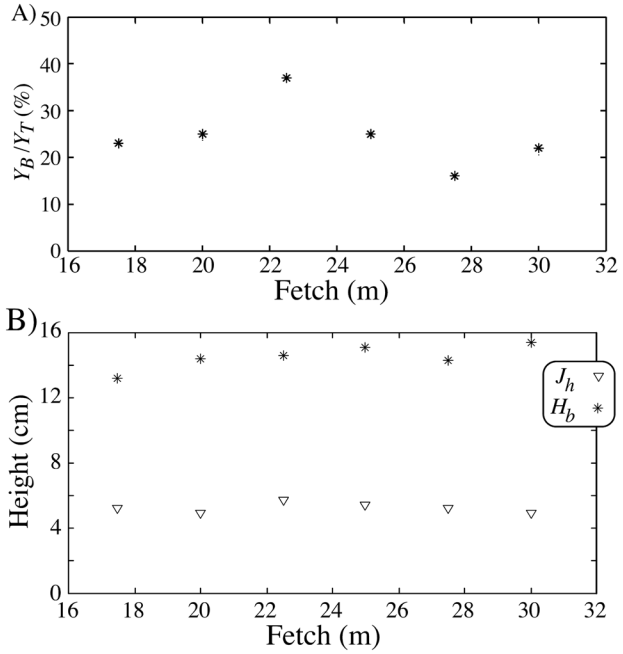

Figure 4. (a) Percent of waves breaking Y_B/Y_T, where Y_T is total number of waves. (b) Average trough-to-crest height and average jump height of the breaking waves versus fetch. These quantities were estimated for the wave signal recorded contemporaneously with the bubble plume observations. Data key is on the figure.

percentage of breaking waves increased again. Also, the standard deviation of H began to increase during this last stage of wave evolution in the channel, indicating a change in the wave group structure (Figure 3). This indicates that the wave field then evolved toward an energy equilibrium with wind after the phase of intense breaking. A more detailed investigation of the wave field with fetch also showed that this well-marked wave evolution with fetch was not only controlled by wave energy wind input or loss by wave breaking but also by the development of skew waves due to wave-wave nonlinear interactions. These skew waves were responsible for large-scale three-dimensional modulation along the tank (with an approximate length scale of 18 m in the longitudinal direction). *Su* [1982] also observed this phenomenon for mechanical waves of high steepness propagating both in an open reservoir and a large tank. Because of cable limitations, the fetches surveyed in this study covered about two-thirds of the wave modulation cycle.

[36] To better characterize the wave breaking intensity, the average height of breaking waves, H_b and the average jump height, J_h, of breaking waves were estimated (Figure 4b). J_h is more precisely defined as the average height of the steep "turbulent" regions observed at the forward face of the breaking wave crests. J_h is a good indicator of the wave energy dissipated by breaking and converted into turbulence and bubble plumes [*Longuet-Higgins and Smith*, 1983; *Caulliez*, 2002].

[37] The average height of the breaking waves varied little with fetch, but reached its highest values in the region where the most active breaking was observed. The evolution of J_h also showed that the most intense breaking occurred in the region near 22.5 m fetch, where it was at a maximum. Downstream of 25 m, H_b and J_h varied less than the mean wave height. This confirmed that in this region the decrease in the breaking activity primarily resulted from a decrease in the wave-breaking rate rather than a decrease in the breaking intensity of the individual breaking waves.

6. Plume Generation

[38] The plume generation rate, P (number of plumes, $m^{-2}\,s^{-1}$), for each plume class was determined at approximately the same fetches as the wave measurements (Figure 5). Also shown is the fetch-averaged P. At the cross-channel location of the NUIG-BMS, wave breaking peaked at 22.5-m fetch (Figure 4). For microplumes and NSDi plumes, P peaked at ~20-m fetch, that is, a few meters upwind of the fetch of maximum wave breaking. After 20-m fetch, P for microplumes and NSDi plumes decreased until 27.5-m fetch, increasing afterward, dramatically for microplumes. The dense plume P peaked at 22.5-m fetch, that is, the fetch of peak wave breaking, thereafter decreasing from 22.5- to 30-m fetch.

[39] At the fetch of maximum wave breaking, there were ~5 plumes produced per wave period (0.8 s), that is, many more than 1 bubble plume per breaking wave. The vast majority of these plumes were diffuse, noninteraction plumes (NSDi and micro). Deep, dense plumes were produced at a rate of less than 1 plume per wave. In the video, there were many occurrences where a series of microplumes and/or NSDi plumes were produced as a series from a single breaking wave. In contrast, only a few dense plumes were produced as a series. Of course, serial production was critical to the generation of the interaction classes.

[40] Over the fetches surveyed, diffuse plumes were produced about three times more frequently than dense plumes. Interestingly, with the accompanying increase both in wave breaking and the total plume generation rate, P_{tot}, at 30-m fetch, microplumes and NSDi plumes were dominant while there were virtually no dense, deep plumes.

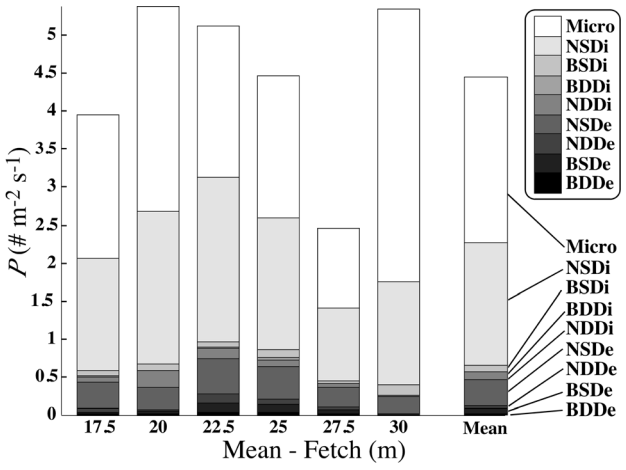

Figure 5. Average plume-class generation rate P versus fetch and averaged over all fetches measured. Classification scheme is described in Table 2.

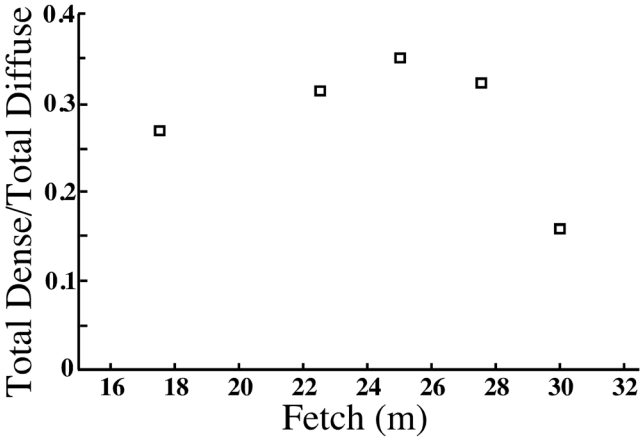

Figure 6. Ratio of dense-to-diffuse plume generation rate (absent microplumes) versus fetch for one experiment. Observations were unavailable at 20-m fetch.

[41] These results suggest that the most important distinction between plume classes was between dense plumes that formed large bubbles and diffuse plumes that largely did not. The fetch dependency of the ratio of P for dense to diffuse plumes (neglecting microplumes) is shown in Figure 6 for one of the experiments. A clear trend of increasing probability of dense plume generation with fetch was observed until 25-m fetch, that is, a few meters downwind of the wave breaking peak (Figure 4a). A shift toward diffuse plumes then followed, first because of the abrupt decrease in the dense plume P, and then at 30-m fetch because of the sharp increase of the diffuse plume P.

7. Total Bubble Plume Bubble Size Distribution

7.1. Injection Plume Bubble Population Size Distribution

[42] LD calculated the injection bubble plume population size distributions, $\Phi_i(r)$, and the time-averaged bubble plume population size distributions, $\Phi_a(r)$, for a set of bubble plumes of each plume class. Combined with the plume-class generation rate, P (Figure 5), and the plume-class lifetime, τ, (Table 3) the local time-averaged, total bubble population, size distribution, $\psi_a(r)$ (number, μm^{-1}) and the local injection, total bubble population size distribution, $\psi_i(r)$ (number, μm^{-1} s^{-1}) were calculated for each fetch by

$$\psi_a = \Sigma[P(X)\Phi_a(X,r)\tau(X)]; \Psi_a = \int \psi_a dA \quad (3)$$

$$\psi_i = \Sigma[P(X)\Phi_i(X,r)]; \ \Psi_i = \int \psi_i dA \quad (4)$$

where X represents the different classes. The global time-averaged, total bubble population size distribution, $\Psi_a(r)$ (number, μm^{-1}) and the global injection, total bubble population size distribution, $\Psi_i(r)$ (number, μm^{-1} s^{-1}), were then calculated by integrating $\psi_a(r)$ and $\psi_i(r)$ over the surveyed area of the channel (between 17.5- and 30-m fetch). Because of the existence of an asymmetry between the left and right sides of the channel (see section 5), this calculation overestimates slightly the total bubble production since the measurements did not cover an entire modulation cycle. Wall effects on wave breaking were small, and thus wall effects on P were neglected.

[43] The local time-averaged, total bubble population size distribution ψ_a for 17.5- and 22.5-m fetch, which corresponded to regions of relatively moderate and high wave development and wave breaking, respectively, are shown in Figure 7. For all r, ψ_a was greater in the region of high wave breaking compared to the region of moderate wave breaking. Furthermore, the ratio of $\psi_a(r)$ between the peak breaking and moderate wave-breaking regions was greater (more bubbles) for $r > 800$ μm. This was consistent with the greater dense plume P at 22.5-m fetch.

[44] The local injection, total bubble population size distribution, ψ_i, as a function of size and fetch is shown in Figure 8a. Large bubble injection peaked at 25-m fetch, corresponding to the peak in the dense plume generation rate (Figure 5), and had a minimum at 27.5-m fetch. The small bubble ψ_i exhibited a smooth maximum between 22.5 and 25 m fetch, a minimum at 27.5-m fetch, and an even higher value at 30-m fetch. Thus the small bubble ψ_i followed the same trend as the diffuse plume P. The global injection, total bubble population size distribution, Ψ_i, for all fetches surveyed is shown in Figure 8b and was well described by two power laws. For $r < 1700$ μm, Ψ_i was well approximated by $\Psi_i \sim r^{-1.2}$ while for larger r, it decreased more steeply as $\Psi_i \sim r^{-3.9}$. Again, note, this is only for one side of the wind wave channel.

[45] The critical r for $\Psi_i(r)$ was ~1700 μm (Figure 8b) and occurred at a larger r than the critical r for diffuse plumes, which was at $r \sim 1000$ μm. Thus the fact that the small-bubble power law extends to larger r can only be explained if the decrease in Φ_i from diffuse plumes for $r >$ 1000 μm was "matched" by the contribution from dense plumes. The contribution to Ψ_i by dense plumes is shown in Figure 8b. As can be seen, the peak in dense plume $\Psi_i(r)$ was at $r \sim 1700$–2000 μm, and matches the decrease in

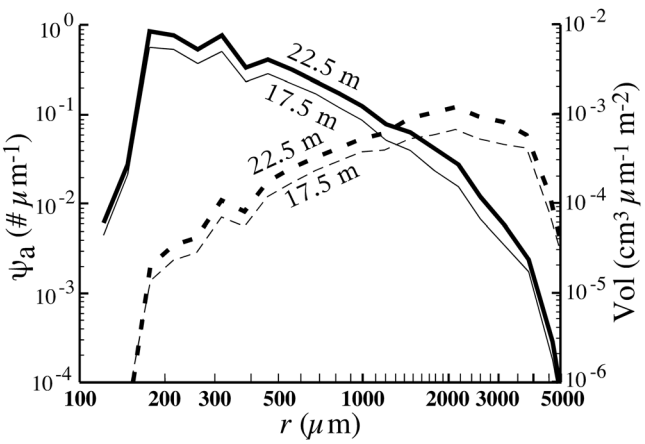

Figure 7. Local time-averaged plume bubble population size distribution ψ_a (solid lines at 17.5- and 22.5-m fetches, representing regions of low and high wave development, respectively, and wave breaking) and the corresponding bubble volume size distribution (dashed lines). Data are labeled on the figure.

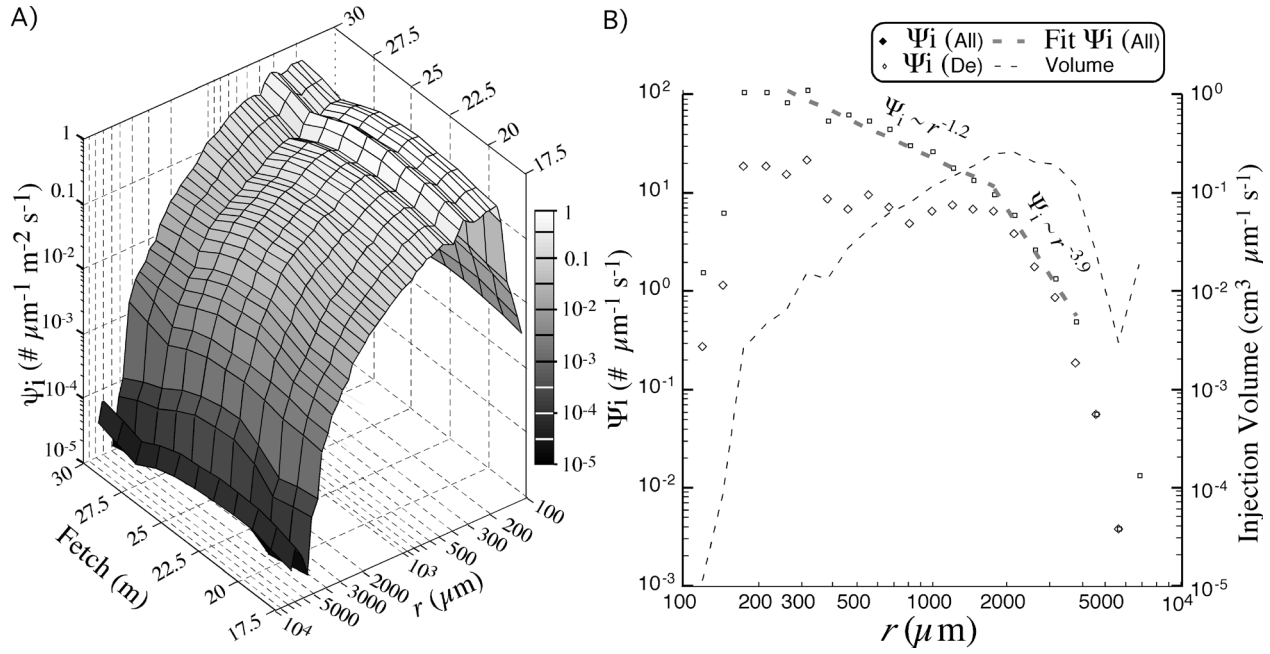

Figure 8. (a) Local injection bubble population size distribution ψ_i rates versus fetch and radius r; ψ_i was linearly interpolated to twice the resolution. (b) Global injection bubble population size distribution Ψ_i versus r for all plumes and only dense plumes, fit, and corresponding volume size distribution. Data key is on the figure.

$\Psi_i(r)$ from diffuse plumes for $r > 1000$ (not shown) yielding the increased critical radius.

[46] With regards to the global injection volume size distribution, both the large and small bubble populations contained roughly half the bubble volume (53% for $r <$ 1700 μm). The maximum in the bubble volume size distribution was at $r \sim 2100$ μm (Figure 8b). Integration of the global injection volume size distribution over r yielded a value of 640 cm^3 of air injected per second into the area surveyed (entire channel width, 12.5 × 2.6 m^2). Bubbles smaller than $r \sim 200$ μm, that is, smaller than the NUIG-BMS resolution limit, contributed negligibly to plume volume. Dense plumes contributed 320 cm^3 of the injected volume, ~56%, or about half.

7.2. Global Bubble Plume Bubble Concentration Size Distribution

[47] Bubble plume distributions were presented in this manuscript and by LD as populations because given the transiency and spatial heterogeneity of bubble plumes, interpretation of a concentration size distribution requires the plume's spatial extent as a function of time, such as would be needed for initialization of a numerical bubble process model [*Leifer*, 1995]. To allow comparison with bubble plume concentration measurements, the global bubble plume bubble size concentration, ϕ_p, was calculated by

$$\phi_p = \{\Sigma[P(X)\Psi_i(X,r)]\}/\{\Sigma[P(X)P_{VM}(X)]\} \quad (5)$$

where P_{VM} is the plume volume at maximum penetration. On the basis of this definition, ϕ_p is the concentration that would be observed by an instrument if it only recorded data when plumes were in its measurement volume, and moreover, this instrument could observe each plume in its entirety (and further assuming no plume overlap at maximum penetration, which would increase ϕ_p). ϕ_p is shown in Figure 9, together with the background concentration size distribution for the same experiments as in this study but measured on the opposite (cross-wind) side of the channel and averaged over the same range of fetches [*De Leeuw and Leifer*, 2002]. For the overlapping bubble size range, at $r \sim 300$ μm, ϕ_p is an order of magnitude higher in the plume than ϕ for the background distribution, and two orders of magnitude greater for $r \sim 500$ μm. Most of the concentration at the larger sizes was contributed by the dense bubble plumes, as shown by the small filled squares in Figure 9. For comparison, ϕ_p from *Deane and Stokes* [2002] for a wind speed of 7 to 10 m s^{-1} at 13°C, is shown. *Deane and Stokes* [2002] reported measurements for individual plumes; for Figure 9, the two highest void fraction plumes (assumed to be closer to formation) were averaged together. Also shown is ϕ for the background population measured in the North Atlantic for 12 to 13 m s^{-1} wind speed and 12°C during the OMEX campaign from *De Leeuw and Cohen* [2002]. A wind speed of 13 m s^{-1} in the tank corresponds to a U_{10} for the ocean of ~17–18 m s^{-1}. Thus the higher equivalent U_{10} probably partially explains why oceanic background concentrations were less than in LUMINY, although comparison between oceanic and LUMINY measurements based solely on wind speed are less than ideal given the dependency of bubble generation on various factors such as fetch, as described above. Although there was no overlapping size range between *De Leeuw and Cohen* [2002] and *Deane and Stokes* [2002], the two distributions suggest that plume bubble concentrations can be three to five orders of magnitude greater than in the

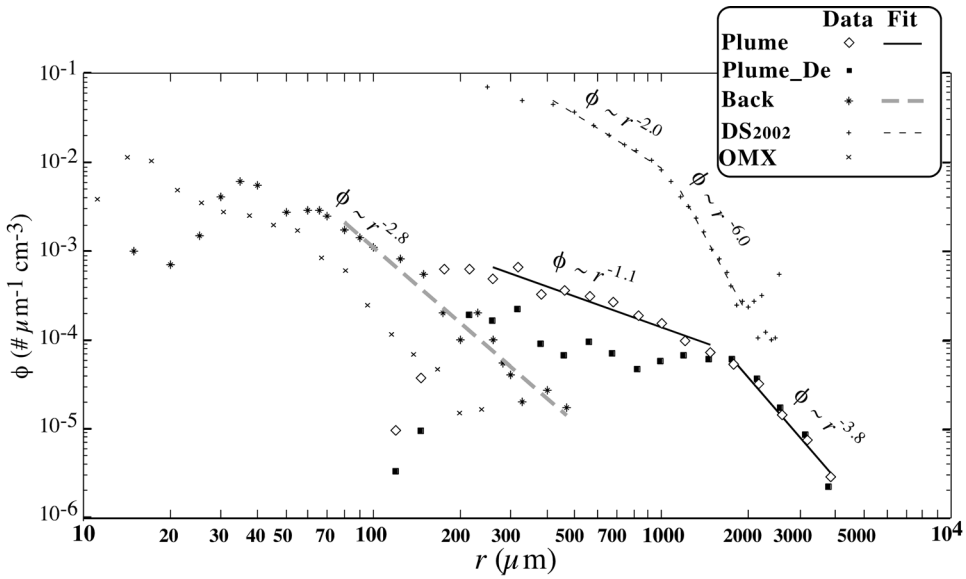

Figure 9. Plume bubble concentration size distribution ϕ_p for bubble plumes, dense plumes, the background distribution, oceanic background bubble plumes (OMX), and oceanic bubble plume bubbles from *Deane and Stokes* [2002]. Data key is on the figure; see text for further details.

background, depending upon r. The caveat, of course, is that the two measurements were taken in different oceans at different times.

8. Discussion

8.1. Bubble Plume Class Distribution Significance

[48] The plume classification approach was developed to address the wide diversity of plume types observed and to preserve the details of the plume populations with regards to the plume attributes. Diffuse plumes (microplumes and NSDi plumes) showed similar trends in P with fetch with the ratio of P between the two favoring microplumes at fetches of lower wave development (e.g., 30-m fetch, Figure 5) and NSDi plumes at fetches where the breaking rate was higher (e.g., 25-m fetch). This similarity in trends was also observed with respect to the bubble size distributions. The bubble size distributions for microplumes and NSDi plumes were very similar, showing a weak size dependency for $r < 1000$ μm, decreasing steeply for larger bubbles. Microplume P peaked at 20 m and then decreased monotonically until 27.5-m fetch. Thus it did not follow closely the trend in wave breaking and wave development. One possibility is obscuration of microplumes by larger dense plumes. However, dense plume P decreased from a peak at 22.5- to 30-m fetch, despite the increase in the breaking rate at 30-m fetch (Figure 4a). This argues that obscuration by dense plumes (which peaked at 22.5-m fetch) was not a significant cause of the decrease in microplume P with fetch. Given their similarity in size distributions, it seems probable that the NSDi and microplume classes resulted from the segregation scheme dividing a single diffuse (noninteraction) plume class in two. The likelihood is that there was a spectrum of diffuse plumes spanning a range of extents and B_I, from microplume size to the largest observed NSDi plumes. Larger diffuse plumes (e.g., NDDi and BDDi) were only due to plume-plume interactions. In this interpretation, there was a shift from the generation of smaller (micro) to larger diffuse plumes (NSDi) with wave development, that is, a shift in the spectrum of plume sizes. In fact, the ratio of microplumes to NSDi plumes (not shown) varied in the same manner as NSDi plumes, decreasing from 20- to 27.5-m fetch, then increasing. Also of note, the diffuse plume P was significant at all fetches with no obvious suppression at the fetch of peak P for dense plumes.

[49] Turbulence intensities in dense plumes likely were greater than for diffuse plumes of similar extent. This was evidenced by the longer lifetime observed for NSDe than for NSDi plumes despite similar extents. The NSDe P showed a similar trend as P for the deeper dense plumes, which were most common in the region of peak wave breaking and wave development. Finally of note was the absence of any intermediate plume classes with respect to density; for example, there was no spectra of plume "optical denseness," which was related to the large bubble peak. In other words, there were no diffuse plumes with a small peak at circa $r \sim 1700$ μm: all diffuse plumes were impoverished in large bubbles. This strongly suggests two different bubble plume and bubble formation mechanisms.

[50] At the shortest fetch, shallow and diffuse plumes dominated, with almost no deep dense plumes. With increasing wave development, dense plumes became more important (22.5- and 25-m fetch). The region of peak wave breaking (22.5 m fetch) correlated with peak wave dissipation (due to wave breaking) after which P decreased for all classes. The sharp decrease in the wave-breaking rate between 22.5- and 25-m fetch probably related to wave dissipation superimposed on the effects of wave modulation. Thus wave modulation can explain the sharp decrease in P at 27.5-m fetch and the shift in plume generation toward less energetic, diffuse plumes.

[51] Clearly, wave breaking and the formation of the more energetic plumes (in terms of z_p and large bubbles) were closely related. In contrast, the relationship between wave

breaking and the probability of diffuse plume formation (as indicated by the ratio of dense to diffuse plumes, for example, Figure 6) was less direct. For example, the ratio of diffuse to dense plume P peaked further downwind than the peak in wave breaking. Also, diffuse plume generation increased at 30-m fetch (due to a significant increase in microplumes) even though wave development had decreased. The increase in the ratio of diffuse to dense plume P at 30-m fetch is in agreement with wave characteristics; however, the overall increase in plume P (albeit diffuse) is puzzling. Here, dense plumes were least important while microplumes and NSDi plumes dominated. One possibility is that there was an area of active, but immature breaking-wave regeneration at 30-m fetch that led to the formation of many small, low-energy plumes. Because small plumes dissipate less energy than larger plumes, this would allow for more small plume formation.

[52] This shift between dense and diffuse plumes occurred at the same fetch where there was a shift between small-scale spilling-type wave breaking (fetches prior to 20 and 30 m) toward plunging-type wave breaking, the fetch of peak wave breaking and maximum jump height. It should be noted that the plumes studied appeared to originate behind the wave crests, and thus may have been produced by a different wave-breaking phenomenon than spilling breakers, whose bubbles were observed trapped in the wave crests. In LUMINY, spilling-wave bubble plumes were formed more or less continuously as the waves traveled downwind, bubbles and plumes from the spilling breakers were visible in the wave crests, but did not penetrate below the wave crest. Bubbles from spilling breakers were not studied in this research.

[53] There were significant differences between the plume and the background bubble populations (Figure 9). For bubbles with $r > 200$, the background ϕ was significantly less than the plume ϕ_p. For large bubbles, the difference was as great as several orders of magnitude. For small bubbles, though, the two appeared to converge. Extrapolation of ϕ_p to small r suggests that ϕ_p and ϕ intersected at $r \sim 50-70$ μm. Since 50-μm bubbles rise at $\sim$0.5 cm s^{-1}, a bubble injected to just 6 cm (z_p for NSDi plumes) requires 12 s to reach the surface. Since the wave frequency was 1.2 Hz and the breaking rate approached as high as 40% (Figure 4a), 50-μm bubbles persisted much longer than the plume formation frequency. In this case, each bubble plume slightly increased the background concentration, which also pervaded the bubble plumes. This phenomenon was reported in a WST experiment for bubbles in this size range [*Leifer*, 1995]. One implication is that S for the small bubble injection concentration size distribution was overestimated (greater than reality) since for each plume, some of the bubbles were reentrained rather than formed by that plume. A bubble's reentrainment probability decreases rapidly with size. For the bubbles in this study, $r >$ 170 μm, which implies $V_B > 3.4$ cm s^{-1} [*Leifer and Patro*, 2002]. For a worst case of a 40% breaking rate of 1.2 Hz waves, this corresponds to a rise from 7 cm, which is greater than z_p for NSDi plumes (6 cm), which are the main source of these small bubbles (Figure 8). Thus the error in the injection distributions presented in this study due to inclusion of entrained background bubbles was small, even at the minimum-size resolution limit.

[54] The primary source of the background population is bubble plumes, although a secondary source is bubble-bursting bubble production that occurs for plume bubbles and background bubbles upon bursting [*Leifer et al.*, 2000c]. Since dense and diffuse plumes have significantly different ϕ, it is likely that this secondary bubble production mechanism also varies with the ratio of diffuse to dense plume P. Also, dense and diffuse plumes likely contributed differently to the background population, because the power law exponent, S, for small bubbles for these plume classes were quite different (shallow for diffuse and steep for dense plumes). Similarly, since most diffuse plumes were shallow, while dense plumes included very deep plumes, the background population should vary with depth because of different sources. Thus some of the variability in S for background concentrations [e.g., *De Leeuw and Cohen*, 2002] may result from differences in the ratio of P for dense and diffuse plumes (or their underlying formation mechanisms). In this study, it was shown that wave development caused a change in the ratio of P for these two classes. Other factors, reviewed in section 1 also probably cause variability in the dense to diffuse ratio of P.

[55] The difference in the injection depth and small bubble ϕ for dense and diffuse plumes may partially explain the observations of *Baldy and Bourgüel* [1987] that the power law exponent of the bubble size distribution increased from $S = 2$ between the wave trough and crest to $S = 4$ below the wave trough, although some of the differences, as discussed above, probably resulted from observations including plumes closer to the formation region.

8.2. Application to the Ocean

[56] Observations within oceanic bubble plumes near the interface by noninvasive techniques are unavailable. The plume bubble size distributions by LD showed a rapid increase in steepness with time and distance from the formation region, which has been observed by others [*Baldy and Bourgüel*, 1987; *Leifer*, 1995; *Haines and Johnson*, 1995; *Deane and Stokes*, 2002], although the distributions by LD were significantly closer to the formation region and time than other published observations.

[57] Clearly oceanic waves have much greater size scales than reproducible in LUMINY. However, evidence suggests that the wave-breaking wavelengths for oceanic waves are much smaller than the dominant wave period, although the dominant waves introduce a modulation of wave breaking [*Dulov et al.*, 2001]. We hypothesize that at higher wind speeds and greater wave development than achievable in LUMINY, there still exists a spectrum of diffuse and dense bubble plumes formed, with the diffuse bubble plumes primarily responsible for the near-surface background bubble population. Also, it seems likely that for higher wind speeds, the increased formation rate of diffuse plumes would cause more plumes of the interaction classes.

[58] These results show a close relationship between the types of plumes formed, the bubble size distribution in the plumes, and the wave-breaking intensity and scale. Small-scale wave breaking tended to produce diffuse plumes, while more intense wave breaking produced both diffuse and dense plumes. Intense wave breaking and the larger

(dense) plumes were associated with a more developed wave field, similar to the inverse relationship between plume penetration depth and wave age observed in the ocean by *Graham et al.* [2004]. We would expect, that underlying this greater plume penetration depth is a shift toward dense plumes which are enriched in large bubbles. Thus, where small-scale wave breaking of nondominant waves occurs [e.g., *Dulov et al.*, 2001] at moderate wind speed or old seas (large c/u^*) – diffuse bubble plumes may be generated preferentially. Where intense wave breaking of the dominant waves occurs [e.g., *Banner et al.*, 2000] for much higher wind speeds, for young seas, or for highly forced-by-wind waves, mainly increasing winds and small c/u^*, dense bubble plumes with larger bubbles may be generated preferentially. Since bubble plumes are the source of the background bubble population, it too should be affected by the wave-breaking intensity and scale. Also, greater injection depth likely causes a stronger size segregation in the injection phase and longer plume lifetimes at higher hydrostatic pressure. That will in turn change the size distribution due to dissolution.

[59] One significant difference between oceanic and LUMINY bubble plumes is salinity (LUMINY was fresh water, albeit not clean). On the basis of the review of the literature presented in section 1, it appears that the large bubble size distribution is essentially independent of salinity effects, (where large is defined as varying from $r > 500$ to $r > 2000$ depending upon the experiment). In contrast, the small bubble size distribution is strongly dependent on salinity. Thus the difference between LUMINY bubbles and oceanic bubbles presumably lies in the "matching" between the large bubble size distribution produced by dense plumes and the small bubble size distribution produced in salt water with a steeper, small bubble size distribution. An example of matching was shown for LUMINY in Figure 9, and was a balance between bubbles produced by dense and diffuse bubble plumes. As a result, the critical radius was extended from $r \sim 1000$ μm for diffuse plumes to $r \sim 1700$ μm for the total global population size distribution. This balancing may not be apparent in published data since few span the critical size range $500 < r < 2500$ μm. The absence of such data results at least in part because both laser and acoustical methods experience difficulties once bubble shapes become irregular because of oscillations ($r > 700$ μm) [*Leifer et al.*, 2000a].

[60] For geophysical bubble modeling of processes such as air-sea gas exchange, the injection or formation bubble size distribution is needed for model initialization [*Memery and Merlivat*, 1985; *Woolf*, 1993; *Keeling*, 1993; *Leifer*, 1995]. It is also important that the model accounts for short-timescale bubble processes. Model initialization with the background bubble population is inappropriate since it is a quasi steady state size distribution of plume remnants and thus is very different from (and much less than) the bubble injection size distribution. Most bubble measurements are of the background population, and unfortunately, a unique injection bubble size distribution cannot be calculated from the background population; that is, different injection distributions can produce the same background population size distribution. The discrepancy between the background and injection size distributions is greater for larger bubbles since their faster rise speeds yields shorter subsurface lifetimes, and thus a greater difference between the steady state background and plume injection populations.

9. Conclusions

[61] To preserve the wide degree of diversity observed in bubble plumes produced by wind and paddle-steepened breaking waves in LUMINY, a plume classification scheme was introduced and the plume characteristics determined for each class. The generation rate for each plume class was analyzed over a range of fetches in the LUMINY wind wave channel. There was a significant distinction between dense and diffuse plumes. Dense plumes had a well-defined peak at $r \sim 1700$ mm which contained most of the bubble mass, while for diffuse plumes, smaller bubbles were more important. The ratio of dense to diffuse plume production varied with fetch and wave development (mean wave height), and favored dense plume production for the region of peak wave breaking. Diffuse plume production varied less with fetch than dense plume production. A local maxima in the diffuse plume production occurred at the fetch of peak wave breaking with a second maxima at a fetch where small-scale wave breaking increased. Because the size distributions for these two plumes were significantly different, the change in the ratio of diffuse to dense plume production caused a change in the global bubble population with wave development. Since the ratio between plume classes and thus bubble distributions varied with wave development, it likely varies with other factors that affect wave development and breaking such as air-water temperature differences, water temperature, and salinity, as indicated by field data.

Notation

r	Equivalent spherical bubble radius, μm.
ϕ	Bubble concentration size distribution, number cm^{-3} μm^{-1}.
S	Power law exponent.
k	Constant, cm^{-3} μm^{+S}.
u,	Wind speed, m s^{-1}.
U_{10}	10-m wind speed, m s^{-1}.
w	Plume horizontal extent, cm.
z_p	Plume penetration depth, cm.
N	Number of bubbles.
τ	Plume lifetime, s.
B_V	Volume of bubbles in the plume, cm^3.
B_{VM},	Maximum B_V, cm^3.
P_{VM},	Plume volume at maximum penetration, cm^3.
H_b	Average height of breaking waves, cm.
J_h	Average jump height of breaking waves, cm.
Y_B	Number of breaking waves, min^{-1}.
Y_T	Number of waves, min^{-1}.
P	Plume generation rate, m^{-2} s^{-1}.
Φ_i	Injection bubble plume population size distribution, number μm^{-1}.
Φ_a	Average bubble plume population size distribution, number μm^{-1}.
$\psi_a(r)$	Local time-averaged total bubble population size distribution, number μm^{-1}.
$\psi_i(r)$	Local injection total bubble population size distribution, number μm^{-1}.

$\Psi_a(r)$ Global time-averaged total bubble population size distribution, number μm^{-1}.
$\Psi_i(r)$ Global injection total bubble population size distribution, number μm^{-1}.
A Surface area, m^2.
X Plume class.
ϕ_p Bubble concentration size distribution in the plume, number cm^{-3} μm^{-1}.
c Wave phase speed, m s^{-1}.
$u*$ Friction velocity, m s^{-1}.

[62] **Acknowledgments.** Most of the work reported here was carried out as part of the LUMINY project, which was supported by the European Commission EC DG XII, contract ENV4-CT95-0080, and as part of TNO, with additional support from the Netherlands Ministry of Defense, assignment A95KM786. Part of the work of Ira Leifer was carried out while he was employed by the National University of Ireland in Galway and when he was a visiting scientist at TNO, while part of the work was performed at the University of California, Santa Barbara, California. The authors would like to thank IRPHE-IOA for the extensive laboratory support provided during LUMINY.

References

Alldredge, A. L., and C. Gotschalk (1990), The relative contribution of marine snow of different origins to biological processes in coastal waters, *Cont. Shelf Res.*, *10*, 41–58.

Alldredge, A. L., U. Passow, and B. E. Logan (1993), The abundance and significance of a class of large, transparent organic particles in the ocean, *Deep Sea Res.*, *40*, 1131–1140.

Asher, W. E., and P. J. Farley (1995), Phase-Doppler anemometer measurement of bubble concentrations in laboratory-simulated breaking waves, *J. Geophys. Res.*, *100*(C4), 7045–7056.

Asher, W. E., L. M. Karle, and B. J. Higgins (1997), On the difference between bubble-mediated air-water transfer in freshwater and seawater, *J. Mar. Res.*, *55*, 813–845.

Backer, L. C., et al. (2003), Recreational exposure to aerosolized brevetoxins during Florida red tide events, *Harmful Algae*, *2*, 19–28.

Baldy, S. (1988), Bubbles in the close vicinity of breaking waves: Statistical characteristics of the generation and dispersion mechanism, *J. Geophys. Res.*, *93*(C7), 8239–8248.

Baldy, S., and M. Bourgüel (1987), Bubbles between the wave trough and wave crest levels, *J. Geophys. Res.*, *92*(C3), 2919–2929.

Banner, M. L., A. V. Babanin, and I. R. Young (2000), Breaking probability for dominant waves on the sea surface, *J. Phys. Oceanogr.*, *30*, 3145–3160.

Baylor, E. R., and W. H. Sutcliffe (1963), Dissolved organic material in seawater as a source of particulate food, *Limnol. Oceanogr.*, *8*, 369–371.

Blanchard, D. C. (1989), The ejection of drops from the sea and their enrichment with bacteria and other materials: A review, *Estuaries*, *12*(3), 127–137.

Blanchard, D. C., and A. H. Woodcock (1957), Bubble formation and modification in the sea and its meteorological significance, *Tellus, Ser. A*, *9*, 145–158.

Boers, R., J. B. Jensen, and P. B. Krummel (1998), Microphysical and radiative structure of marine stratocumulus clouds over the Southern Ocean: Summer results and seasonal differences, *Q. J. R. Meteorol. Soc.*, *124*, 151–168.

Cartmill, J. W., and Y.-M. Su (1993), Bubble size distributions under saltwater and freshwater breaking waves, *Dyn. Atmos. Oceans*, *20*, 25–31.

Caulliez, G. (2002), Statistics of geometric properties of breaking wind waves observed in the laboratory, in *Gas Transfer at Water Surfaces*, *Geophys. Monogr. Ser.*, vol. 127, edited by M. Donelan et al., pp. 31–37, AGU, Washington, D. C.

Cincinelli, A., A. M. Stortini, M. Pergini, L. Checchini, and L. Lepri (2001), Organic pollutants in sea-surface microlayer and aerosol in the coastal environment of Leghorn— (Tyrrhenian Sea), *Mar. Chem.*, *76*, 77–98.

Cini, R., and G. Loglio (1997), Adsorption and pollutant transport by marine aerosol, *Mar. Pollut. Bull.*, *34*(7), 501–504.

Clift, R., J. R. Grace, and M. E. Weber (1978), *Bubbles, Drops, and Particles*, 380 pp., Elsevier, New York.

Crawford, G. B., and D. M. Farmer (1987), On the spatial distribution of ocean bubbles, *J. Geophys. Res.*, *92*(C8), 8231–8243.

Dam, H. G., and D. T. Drapeau (1995), Coagulation efficiency, organic-matter glues and the dynamics of particles during a phytoplankton bloom in a mesocosm study, *Deep Sea Res., Part II*, *42*, 111–123.

Deane, G. B., and M. D. Stokes (2002), Scale dependence of bubble creation mechanisms in breaking waves, *Nature*, *418*, 839–843.

Deglon, D. A., F. Sawyerr, and C. T. O'Connor (1999), A model to relate the flotation rate constant and the bubble surface area flux in mechanical flotation cells, *Miner. Eng.*, *12*, 599–608.

De Leeuw, G. (1990), Spray droplet source function: From laboratory to open ocean, in *Modeling the Fate and Influence of Marine Spray*, edited by P. G. Mestayer, E. C. Monahan, and P. A. Beetham, *Whitecap Rep. 7*, pp. 17–28, Univ. of Conn., Groton.

De Leeuw, G. (1993), Aerosols near the air-sea interface, *Trends Geophys. Res.*, *2*, 55–70.

De Leeuw, G., and L. H. Cohen (2002), Bubble size distributions on the North Atlantic and North Sea, in *Gas Transfer at Water Surfaces*, *Geophys. Monogr. Ser.*, vol. 127, edited by M. Donelan et al., pp. 271–277, AGU, Washington, D. C.

De Leeuw, G., and I. Leifer (2002), Bubbles outside the bubble plume during the LUMINY wind-wave experiment, in *Gas Transfer at Water Surfaces*, *Geophys. Monogr. Ser.*, vol. 127, edited by M. Donelan et al., pp. 295–301, AGU, Washington, D. C.

De Leeuw, G., et al. (2002), LUMINY—An overview, in *Gas Transfer at Water Surfaces*, *Geophys. Monogr. Ser.*, vol. 127, edited by M. Donelan et al., pp. 291–294, AGU, Washington, D. C.

De Leeuw, G., et al. (2003), Deposition of nitrogen into the North Sea, *Atmos. Environ.*, *37*, 145–165.

Dulov, V. A., V. N. Kudryavtsev, and A. N. Bol'shakov (2001), A field study of whitecap coverage and its modulations by energy containing surface waves, in *Gas Transfer at Water Surfaces*, *Geophys. Monogr. Ser.*, vol. 127, edited by M. Donelan et al., pp. 187–192, AGU, Washington, D. C.

Fdhila, R. B., and P. C. Duineveld (1996), The effect of surfactant on the rise of a spherical bubble at high Reynolds and Peclet numbers, *Phys. Fluids*, *8*, 310–321.

Flatau, P. J., M. Flatau, J. R. V. Zaneveld, and C. D. Mobley (2000), Remote sensing of bubble clouds in sea water, *Q. J. R. Meteorol. Soc.*, *126*, 2511–2523.

Gemmrich, J. R. (2000), Temperature anomalies beneath breaking waves and the decay of wave-induced turbulence, *J. Geophys. Res.*, *105*(C4), 8727–8736.

Gemmrich, J. R., and D. M. Farmer (1999), Observations of the scale and occurrence of breaking surface waves, *J. Phys. Oceanogr.*, *29*, 2595–2606.

Graham, A., D. K. Woolf, and A. J. Hall (2004), Aeration due to breaking waves. part 1: Bubble populations, *J. Phys. Oceanogr.*, *34*, 989–1007.

Grammatika, M., and W. B. Zimmerman (2001), Microhydrodynamics of flotation processes in the sea surface layer, *Dyn. Atmos. Oceans*, *34*, 327–348.

Grzebyk, D., A. Denardou, B. Berland, and Y. F. Pouchus (1997), Evidence of a new toxin in the red-tide dinoflagellate *Prorocentrum minimum*, *J. Plankton Res.*, *19*(8), 1111–1124.

Haines, M. A., and B. D. Johnson (1995), Injected bubble populations in seawater and fresh water measured by a photographic method, *J. Geophys. Res.*, *100*(C4), 7057–7068.

Hwang, P. A., Y.-H. L. Hsu, and J. Wu (1990), Air bubbles produced by breaking wind waves: A laboratory study, *J. Phys. Oceanogr.*, *20*, 19–28.

Intergovernmental Panel on Climate Change (2001), *Climate Change 2001: The Scientific Basis*, edited by J. T. Houghton et al., Cambridge Univ. Press, New York.

Johnson, B. D., and R. C. Cooke (1979), Bubble populations and spectra in coastal waters: A photographic approach, *J. Geophys. Res.*, *84*(C7), 3761–3766.

Johnson, B. D., X. Zhou, and P. J. Wangersky (1986), Surface coagulation in sea water, *Neth. J. Sea Res.*, *20*, 201–210.

Keeling, R. F. (1993), On the role of large bubbles in air-sea gas exchange and supersaturation in the ocean, *J. Mar. Res.*, *51*, 237–271.

Kepkay, P. E. (1991), Surface coagulation and microbial respiration in response to local advection and sea state in the North Atlantic, *Mar. Ecol. Prog. Ser.*, *69*, 143–147.

Kitaigorodskii, S. A. (1984), Wind-wave effects on gas transfer, in *Gas Transfer at Water Surfaces*, edited by W. Brutsaert and G. H. Jirka, pp. 141–170, Springer, New York.

Kolovayev, P. A. (1976), Investigation of the concentration and statistical size distribution of wind-produced bubbles in the near-surface ocean layer, *Oceanology*, Engl. Trans., *15*, 659–661.

Leifer, I. S. (1995), A validation study of bubble mediated air-sea gas transfer modeling, Ph.D. thesis, Ga. Inst. of Technol., Atlanta.

Leifer, I., and G. De Leeuw (2006), Bubbles generated from wind-steepened breaking waves: 1. Bubble plume bubbles, *J. Geophys. Res.*, *111*, C06020, doi:10.1029/2004JC002673.

Leifer, I., and R. Patro (2002), The bubble mechanism for transport of methane from the shallow sea bed to the surface: A review and sensitivity study, *Cont. Shelf Res.*, *22*, 2409–2428.

Leifer, I. S., R. K. Patro, and P. Bowyer (2000a), A study on the temperature variation of rise velocity for large clean bubbles, *J. Atmos. Oceanic Technol.*, *17*(10), 1392–1402.

Leifer, I., J. Clark, and R. Chen (2000b), Modifications of the local environment by a natural marine hydrocarbon seep, *Geophys. Res. Lett.*, *27*(22), 3711–3714.

Leifer, I., G. De Leeuw, and L. H. Cohen (2000c), Secondary bubble production from breaking waves: The bubble burst mechanism, *Geophys. Res. Lett.*, *27*(24), 4077–4080.

Leifer, I., G. De Leeuw, and L. H. Cohen (2003), Optical measurement of bubbles: System design and application, *J. Atmos. Oceanic Technol.*, *20*(9), 1317–1332.

Liss, P. S., et al. (1997), Physical processes in the microlayer and the air-sea exchange of trace gases, in *The Sea Surface and Global Change*, edited by P. S. Liss and R. A. Duce, pp. 1–33, Cambridge Univ. Press, New York.

Loewen, M. R., M. A. O'Dor, and M. G. Skafel (1996), Bubbles entrained by mechanically generated breaking waves, *J. Geophys. Res.*, *101*(C9), 20,759–20,770.

Longuet-Higgins, M. S., and N. D. Smith (1983), Measurement of breaking by a surface jump meter, *J. Geophys. Res.*, *88*, 9823–9831.

Mao, L., and R.-H. Yoon (1997), Predicting flotation rates using a rate equation derived from first principles, *Int. J. Miner. Proc.*, *51*(1), 171–181.

Mari, X. (1999), Carbon content and C:N ratio of transparent exopolymeric particles (TEP) produced by bubble exudates of diatoms, *Mar. Ecol. Prog. Ser.*, *183*, 59–71.

Marks, R., K. Kruczalak, K. Jankowska, and M. Michalska (2001), Bacteria and fungi in air over the Gulf of Gdansk and Baltic Sea, *J. Aerosol Sci.*, *32*, 237–250.

Mårtensson, E. M., E. D. Nilsson, G. de Leeuw, L. H. Cohen, and H.-C. Hansson (2003), Laboratory simulations and parameterization of the primary marine aerosol production, *J. Geophys. Res.*, *108*(D9), 4297, doi:10.1029/2002JD002263.

Medwin, H., and N. D. Breitz (1989), Ambient and transient bubble spectral densities in quiescent seas and under spilling breakers, *J. Geophys. Res.*, *94*(C9), 12,751–12,759.

Memery, L., and L. Merlivat (1985), Modelling of gas flux through bubbles at the air-water interface, *Tellus, Ser. B*, *37*, 272–285.

Monahan, E. C. (1986), The ocean as a source for atmospheric particles, in *The Role of Air-Sea Exchange in Geochemical Cycling*, edited by P. Buat-Menard, pp. 129–163, Springer, New York.

Monahan, E. C., and H. G. Dam (2001), Bubbles: An estimate of their role in the global oceanic flux of carbon, *J. Geophys. Res.*, *105*(C5), 9377–9383.

Mopper, K., J. A. Zhou, K. S. Ramana, U. Passow, H. G. Dam, and D. T. Drapeau (1995), The role of surface-active carbohydrates in the flocculation of a diatom bloom in a mesocosm, *Deep Sea Res., Part II*, *42*, 47–73.

O'Dowd, C. D., J. A. Lowe, and M. H. Smith (1999a), Coupling of sea-salt and sulphate interactions and its impact on cloud droplet concentration predictions, *Geophy. Res. Lett.*, *26*(9), 1311–1314.

O'Dowd, C. D., J. A. Lowe, and M. H. Smith (1999b), Observations and modelling of aerosol growth in marine stratocumulus, *Atmos. Environ.*, *33*, 3053–3062.

O'Dowd, C. D., J. A. Lowe, N. Clegg, M. H. Smith, and S. L. Clegg (2000), Modeling heterogeneous sulphate production in maritime stratiform clouds, *J. Geophys. Res.*, *105*(D6), 7143–7160.

O'Dowd, C. D., M. C. Facchini, F. Cavalli, D. Ceburnis, M. Mircea, S. Decesari, S. Fuzzi, Y. J. Yoon, and J. P. Putaud (2004), Biogenically driven organic contribution to marine aerosol, *Nature*, 676–680, doi:10.1038/nature02959.

Passow, U. (2000), Formation of transparent exopolymer particles, TEP, from dissolved precursor material, *Mar. Ecol. Prog. Ser.*, *192*, 1–11.

Passow, U., A. L. Alldredge, and B. E. Logan (1994), The role of particulate carbohydrate exudates in the flocculation of diatom blooms, *Deep Sea Res., Part II*, *41*, 335–357.

Patro, R. K., I. Leifer, and P. Bowyer (2002), Better bubble process modeling: Improved bubble hydrodynamics parameterization, in *Gas Transfer at Water Surfaces*, *Geophys. Monogr. Ser.*, vol. 127, edited by M. Donelan et al., pp. 315–320, AGU, Washington, D. C.

Persechini, M. A. M., F. G. Jota, and A. E. C. Peres (2000), Dynamic model of a flotation column, *Miner. Eng.*, *13*, 1465–1481.

Pierce, R. H., M. S. Henry, L. S. Profitt, and P. A. Hasbrouck (1990), Red tide toxin (brevetoxin) enrichment in marine aerosol, in *Toxic Marine Phytoplankton*, edited by E. Graneli et al., pp. 128–131, Elsevier, New York.

Pierce, R. H., M. S. Henry, P. C. Blum, S. L. Hamel, B. Kirkpatrick, and Y. S. Cheng (2005), Brevetoxin composition in water and marine aerosol along a Florida beach: Assessing potential human exposure to marine biotoxins, *Harmful Algae*, *4*, 965–972.

Rumbold, D., and S. Snedaker (1999), Sea-surface microlayer toxicity off the Florida Keys, *Mar. Environ. Res.*, *47*(5), 457–472.

Sadhal, S., and R. E. Johnson (1983), Stoke's flow past bubbles and drops partially coated with thin films, *J. Fluid Mech.*, *126*, 237–250.

Spiel, D. (1998), On the births of film drops from bubbles bursting on seawater surfaces, *J. Geophys. Res.*, *103*(C11), 24,907–24,918.

Spillane, M. C., E. C. Monahan, P. A. Bowyer, D. M. Doyle, and P. J. Stabeno (1986), Whitecaps and global fluxes, in *Oceanic Whitecaops*, edited by E. C. Monahan and G. MacNiocaill, pp. 209–218, Springer, New York.

Stramska, M., R. Marks, and E. C. Monahan (1990), Bubble-mediated aerosol production as a consequence of wave breaking in supersaturated (hyperoxic) seawater, *J. Geophys. Res.*, *95*(C10), 18,281–18,288.

Su, M. (1982), Three-dimensional deep-water waves. part 1. Experimental measurement of skew and symmetric wave patterns, *J. Fluid Mech.*, *124*, 73–108.

Terrill, E. J., W. K. Melville, and D. Stramski (2001), Bubble entrainment by breaking waves and their influence on optical scattering in the upper ocean, *J. Geophys. Res.*, *106*(C8), 16,815–16,823.

Thorpe, S. A. (1982), On the clouds of bubbles formed by breaking wind-waves in deep water and their role in air-sea gas transfer, *Philos. Trans. R. Soc. London, Ser. A*, *304*, 155–210.

Thorpe, S. A., P. Bowyer, and D. K. Woolf (1992), Some factors affecting the size distributions of oceanic bubble, *J. Phys. Oceanogr.*, *22*, 382–389.

Vagle, S. V., and D. M. Farmer (1992), The measurement of bubble size distributions with acoustical backscatter, *J. Atmos. Oceanic Technol.*, *9*, 630–644.

Vagle, S. V., and D. M. Farmer (1998), A comparison of four methods of bubble size and void fraction measurements, *IEEE J. Oceanic Eng.*, *23*, 211–222.

Van der Pol, L. A., I. Paijens, and J. Tramper (1995), Dextran as protectant against damage caused by sparging for hybridoma cells in a bubble column, *J. Biotechnol.*, *43*, 103–110.

Van Dolah, F. M., D. Roelke, and R. M. Greene (2001), Health and ecological impacts of harmful algal blooms: Risk assessment needs, *Hum. Ecol. Risk Assess*, *7*(5), 1329–1345.

Walsh, A. L., and P. J. Mulhearn (1987), Photographic measurements of bubble populations from breaking wind waves at sea, *J. Geophys. Res.*, *92*(C13), 14,553–14,565.

Wanninkhof, R. (1992), Relationship between wind speed and gas exchange over the ocean, *J. Geophys. Res.*, *97*(C5), 7373–7382.

Woolf, D. K. (1993), Bubbles and the air-sea transfer velocity of gases, *Atmos. Ocean*, *31*(4), 517–540.

Woolf, D. K. (1997), Bubbles and their role in gas exchange, in *The Sea Surface and Global Change*, edited by P. S. Liss and R. A. Duce, pp. 174–205, Cambridge Univ. Press, New York.

Wu, J. (1988), Bubbles in the near surface ocean: A general description, *J. Geophys. Res.*, *93*(C1), 587–590.

Wu, J. (1995), Mechanisms of animal cell damage associated with gas bubbles and cell protection by medium additives, *J. Biotechnol.*, *43*, 81–94.

Wu, J. (2000), Bubbles produced by breaking waves in fresh and salt waters, *J. Phys. Oceanogr.*, *30*, 1809–1813.

G. Caulliez, Institut de Recherche sur les Phenomenes Hors Equilibre, 163 avenue de Luminy, Case 903, F-13288 Marseille Cedex 9, France. (guillemette.caulliez@irphe.univ-mrs.fr)

G. de Leeuw, TNO Physics and Electronics Laboratory, P.O. Box 96864, NL-2509 JG, The Hague, Netherlands. (deleeuw@fel.tno.nl)

I. Leifer, Marine Science Institute, University of California, Santa Barbara, CA 93106-5080, USA. (ira.leifer@bubbleology.com)